

# High-static–low-dynamic Stiffness Isolator with Tunable Electromagnetic Mechanism

Yi Sun<sup>#</sup>, *Member, IEEE*, Jinglei Zhao<sup>#</sup>, Min Wang, Yu Sun, *Fellow, IEEE*, Huayan Pu<sup>\*</sup>, Jun Luo, Yan Peng, Shaorong Xie, and Yi Yang

**Abstract**—A high-static–low-dynamic stiffness (HSLDS) vibration isolator based on a tunable nesting-type electromagnetic negative stiffness (NS) mechanism is presented. The stiffness characteristics of the HSLDS system can be tuned by regulating the current in the coil. When the current is zero, the HSLDS system may degenerate into a passive isolator. The distinctive features of this proposed isolation system are demonstrated from two aspects: (1) in contrast to passive isolators, the proposed isolator can further widen the bandwidth of vibration isolation and improve the isolation performance near the natural frequency of the passive system; (2) compared with certain other electromagnetic isolation systems, the proposed system has a more compact structure, heavier load capacity, and higher NS-generating efficiency. The proposed electromagnetic NS mechanism consists of four permanent magnets and four coil windings. Analytical models of the electromagnetic force and the displacement transmissibility are established. To select an appropriate structural parameter for the prototype, the effects of geometric parameters on transmissibility are discussed from a theoretical viewpoint. The vibration isolation performance of the proposed isolator system is verified, and a tuning strategy is investigated through experiments.

**Index Terms**—High-static–low-dynamic stiffness, Electromagnetic negative stiffness, Vibration isolation

## I. INTRODUCTION

**M**ECHANICAL vibration is a naturally occurring phenomenon that exists in many aspects of the industry. Therefore, vibration isolation equipment is critical to industrial systems [1–3] and numerous vibration control [4–7] technologies have been investigated in detail. Generally, for passive vibration isolators, which usually consist of linear springs and viscous dampers, there is a trade-off between the load capacity and the vibration attenuation performance. To a linear system, vibration isolation occurs in the frequency zone that is greater than  $\sqrt{2}$  times the natural frequency of the system. Thus, in order to improve the isolation performance from the perspective of broadening the isolation range and improving

the transmissibility characteristic near the resonance zone, one of the most direct approaches is to lower the natural frequency, namely, to reduce the equivalent/overall stiffness of the isolator. However, for passive systems, the stiffness cannot be reduced infinitely because large static deformation may be caused. Therefore, a novel vibration isolator, which is referred to as a high-static–low-dynamic stiffness (HSLDS) isolator [8–10], is investigated by introducing negative stiffness (NS) [11–16].

Several methods are employed to achieve NS. A common method is to connect a vertical spring with two horizontal/oblique springs [17], in which the oblique springs provide NS once the isolated mass deviates from the equilibrium position. Other methods include utilizing the magnetic force between permanent magnets [18–20], utilizing brackets and hinges to construct an NS corrector [21], or employing four oblique buckled Euler beams to provide NS [22].

However, even though oblique springs and buckled beams can realize the HSLDS, the structure is relatively large because of their layouts. This may restrict the application range if the system installation space available is limited. In addition, for traditional mechanical (e.g., oblique springs and buckled beams) and magnetic (e.g., tile magnets) HSLDS systems, it is difficult to adjust the characteristics with respect to external excitation once the structural dimensions are fixed, which may weaken the adaptability for different vibration sources. Compared with mechanical or magnetic variable stiffness systems, electromagnetic devices have two advantages: first, the non-contact characteristic of the electromagnetic force can not only lead to a more compact mechanical structure, but also a longer fatigue life; second, the electromagnetic NS can be varied by tuning the current in coil windings, which makes it possible to optimize the system online in order to prevent a degradation in the attenuation performance.

Therefore, electromagnet-based isolators with smaller size and can be tuned online have attracted the attention of several researchers. Ledezma et al. [10, 23] devised an electromagnetic shock isolator. Zhou et al. [24, 25] proposed an HSLDS electromagnetic isolator. Both these creative works use oblique components (nylon wire/steel beam) to provide positive stiffness (PS), which restricts their structural compactness in the axial plane. In addition, as static deformation is inevitable making it difficult to adjust the equilibrium positions for nylon wires or steel beams, these systems are suitable for horizontal mounting, which degrades their load capacity. Moreover, their separated sandwich-type structure also expands their effective volume (the volume of the part that generates NS). If the

Y. Sun, J. Zhao, M. Wang, H. Pu, J. Luo, Y. Peng, S. Xie and Y. Yang are with the School of Mechatronics Engineering and Automation, Shanghai University, Shanghai, China.

Y. Sun is with Department of Mechanical and Industrial Engineering, University of Toronto, Toronto, M5S 3G8, Canada.

<sup>#</sup>These authors contributed equally. This work was supported by the National Natural Science Foundation of China under Grants 51575329, 61773254, 61625304 and 61873157; in part by Shanghai Rising-Star Program under Grants 17QA1401500; in part by Science and Technology Commission of Shanghai under Grants 16441909400 and 17DZ1205000.

<sup>\*</sup>Corresponding author: H. Pu (email: phygood\_2001@shu.edu.cn).

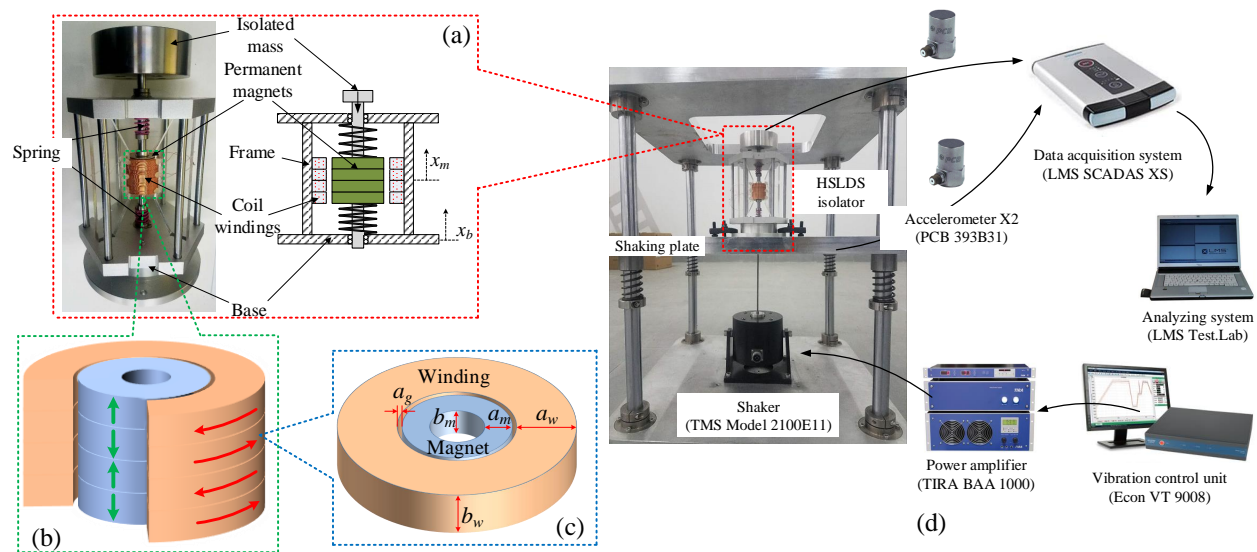


Fig. 1. Experimental setup of the proposed isolator: (a) HSLDS system; (b) electromagnetic mechanism, where the green and red arrow represent the magnetization direction and the polarity of current, respectively; (c) coil winding (CW) and permanent magnet (PM); (d) experimental setup.

payload carried per unit effective volume is regarded as an index of efficiency, smaller effective volumes and heavier payloads are preferable from the perspective of engineering.

Thus, inspired by the pioneering studies of Zhou and Ledezma, this work aims to develop a tunable HSLDS isolator by utilizing a novel electromagnetic NS mechanism, which has a more compact design, heavier load capacity, and higher efficiency of isolation. Instead of the separated sandwich-type mechanism, we proposed a novel electromagnetic NS mechanism by nesting permanent magnets (PMs) within coil windings (CWs). This nesting-type layout makes the structure more compact and facilitates the integration of more PMs or CWs within a limited space to increase NS. PS is provided by two parallel mechanical springs, through which the equilibrium position can be easily controlled by adjusting the preload of the springs, regardless of vertical or horizontal mounting. Therefore, a large load capacity can be realized. Consequently, the efficiency is improved as isolation of a heavier load can be realized through a smaller effective volume. In addition, a systematic tuning strategy is developed to achieve a higher vibration attenuation performance than those of passive systems or pure HSLDS systems. The generality of this system warrants its direct use in guiding the design and parameter selections of other HSLDS systems.

## II. HSLDS SYSTEM DESCRIPTION

To construct an electromagnetic HSLDS isolation system with a compact design and high isolation efficiency, we proposed a nesting-type electromagnetic mechanism, which is composed of four ring PMs and four CWs (Fig. 1a). The axial thickness of the PMs and the CWs are equal since the interaction force/stiffness will be the largest in this configuration according to literatures [9, 26]. All the PMs are axially magnetized and the magnetization directions of the adjacent PMs, as well as the directions of the current in adjacent CWs, are opposite. Two shaft collars are utilized to

remain the PMs in contact with adjacent ones, and to fasten these four PMs at a specific position on the shaft. The CWs are stuck to the inner wall of the frame, and there exists a clearance between the PMs and the CWs to ensure non-interference of movement between them. It is noteworthy that the clearance is an important parameter that may influence the magnetic flux density, hence the magnitude of the electromagnetic interaction force/stiffness. Thus, it will be discussed in detail and selected in the later section. Once it is determined, it remains a fixed value during the operation because there is no movement in radial direction for the PMs. Fig. 1a also shows the equilibrium position of the isolator, at which the equivalent stiffness is the lowest. Thus, in order to achieve the maximum isolation effect, the center plane of the PMs should coincide with that of the CWs axially.

An apparent feature of this mechanism is that the PMs are nested into the CWs (Fig. 1b-c), which is beneficial for reducing the dimensions of the overall structure. Furthermore, owing to the nesting-type layout and the use of mechanical springs, the effective volume is small, and the load capacity is significant. Consequently, the load carried by per unit effective volume increases. To further maximize the isolation performance, on the basis of the nesting-type layout, we proposed a design procedure to derive the optimum structural parameters (listed in Table I) in the following section. The main objectives are to: (1) decrease the natural frequency to broaden the frequency range that isolation occurs; (2) lower the peak transmissibility to decrease the influence of the base vibration on the payload.

Materials for the prototype include aluminum and acrylic plexiglass. The CWs are fixed to the base of the isolator, and the PMs are connected to the isolated mass through a shaft. Sliding bearings are equipped to decrease the friction between the base and the shaft and to ensure that the shaft can only move vertically. Fig. 1d shows a schematic of the experimental setup. The prototype is mounted on a shaking platform



TABLE I  
STRUCTURAL PARAMETERS AND VARIABLES OF THE SYSTEM

Structural Parameters			
Parameter	Value	unit	Definition
$r_c, R_c$	15.8, 23.5	mm	Inner / outer radius of the CW.
$r_m, R_m$	5, 15	mm	Inner / outer radius of the PM.
$N_m$	50	-	Number of turns axially of the PM.
$N_z, N_r$	18, 16	-	Number of turns axially / radially of the CW.
$a_m, a_w$	10, 7.7	mm	Radial thickness of the PM / CW.
$b_m, b_w$	10, 10	mm	Axial thickness of the PM / CW.
$a_g$	0.8	mm	Clearance.
$B_r$	1.35	T	Magnetization of the PM.
$D_a$	-	mm	Axial clearance between adjacent CWs.
$m$	3.519	kg	Mass of the payload.
$c$	0.017	Ns/mm	Equivalent damping of the system.
$\xi$	0.044	-	Equivalent damping ratio of the system.
$k_s$	5.4	N/mm	Stiffness of the mechanical spring.
Variables			
$f, f^*$	-	N	Total / electromagnetic force
$p_1, p_3$	-	-	Fitting parameters of the NS.
$k_1, k_3$	-	N/mm	Linear / cubic stiffness of the system
$I_1$	-	A	Excited current in CWs.
$I_2$	-	A	Equivalent current of the PM.
$X_b$	-	mm	Excitation amplitude of the base.
$\theta$	-	rad	Phase of the response.
$x_b, x_m$	-	mm	Displacement of the base / mass.
$\hat{x}_b, \hat{x}_m$	-	-	Dimensionless displacement of the base / mass.
$x$	-	mm	Relative displacement.
$\omega_b$	-	rad/s	Excitation frequency of the base.
$\omega_n, \omega_h$	-	rad/s	Natural frequency of the passive system (without NS) / HSLDS system (with NS).
$T_n, T_h$	-	-	Peak transmissibility of the passive system (without NS) / HSLDS system (with NS).
$\hat{X}$	-	-	Dimensionless amplitude of the mass.
$\alpha, \gamma$	-	-	Dimensionless linear / cubic stiffness.
$\beta$	-	-	Dimensionless excitation frequency.
$\tau$	-	-	Dimensionless time.
$R_a, R_r, R_g$	-	-	Axial thickness ratio, radial thickness ratio and clearance ratio.
$k^2$	-	-	Modulus.
$K, E$	-	-	Complete first / second elliptic integrals.
$r_1, r_2$	-	mm	Radius of filaments.
$\mu_0$	$4\pi e-7$	H/m	Permeability of vacuum.
$L$	-	mm	Distance between two filaments.

#### IV. DYNAMIC ANALYSIS

The dynamic characteristics of the HSLDS isolator will be investigated in this section. All the symbols used here are listed and explained in Table I, and hence, they will not be explained in detail below.

##### A. Motion equation

The sum of the spring force and the electromagnetic force is

$$f = (2k_s - p_1)x - p_3x^3 \quad (3)$$

Thus, the motion equation of the isolator under an external displacement excitation  $x_b = X_b \cos \omega_b t$  at the base is

$$m\ddot{x} + c\dot{x} + k_1x + k_3x^3 = -m\ddot{x}_b \quad (4)$$

where the dots denote the derivatives with respect to time  $t$ ,  $k_1 = 2k_s - p_1$  is the linear stiffness;  $k_3 = -p_3$  is the cubic

nonlinear stiffness. Thus, the motion equation can be further non-dimensionalized as

$$\hat{x}'' + 2\xi\hat{x}' + \alpha\hat{x} + \gamma\hat{x}^3 = \beta^2 \cos \beta\tau \quad (5)$$

where the primes denote the derivatives with respect to dimensionless time  $\tau$ , and

$$\xi = \frac{c}{2m\omega_n}, \alpha = \frac{k_1}{2k_s}, \gamma = \frac{k_3X_b^2}{2k_s}, \hat{x} = \frac{x}{X_b}, \beta = \frac{\omega_b}{\omega_n}, \omega_n = \sqrt{\frac{2k_s}{m}}$$

The harmonic balance (HB) method [16, 19, 20], which is usually applied to obtain the periodic solution approximately, is adopted to solve the above nonlinear differential equations. The solution to the equation indicates the steady-state response of the mass under a given excitation of the base. According to the HB method, assuming that the high order terms (greater than the first order) in the solution have little influence on the steady-state response and hence can be neglected. Then, we can derive the first order periodic solution of (5) by assuming that it has a form of  $\hat{x} = \hat{X} \cos(\beta\tau + \theta)$ . Substituting it into (5), neglecting the terms containing  $3(\beta\tau + \theta)$ , and after simple reduction, the following amplitude-frequency response can be obtained

$$\begin{cases} -\beta^2 \hat{X} + \alpha \hat{X} + \frac{3}{4} \gamma \hat{X}^3 = \beta^2 \cos \theta \\ -2\xi \hat{X} \beta = \beta^2 \sin \theta \end{cases} \quad (6)$$

The above equation can be further simplified as

$$\left[ (\alpha - \beta^2) \hat{X} + \frac{3}{4} \gamma \hat{X}^3 \right]^2 + (-2\xi \hat{X} \beta)^2 = \beta^4 \quad (7)$$

##### B. Displacement transmissibility

The amplitude  $\hat{X}$  can be calculated numerically through (7). Because the dimensionless absolute displacement of the base is  $\hat{x}_b = \cos \beta\tau$ , the dimensionless absolute displacement of the mass  $\hat{x}_m$ , which equals to the sum of  $\hat{x}_b$  and  $\hat{x}$ , can be expressed as

$$\begin{aligned} \hat{x}_m &= \hat{x}_b + \hat{x} = \cos \beta\tau + \hat{X} \cos(\beta\tau + \theta) \\ &= (1 + \hat{X} \cos \theta) \cos \beta\tau - \hat{X} \sin \theta \sin \beta\tau \end{aligned} \quad (8)$$

The displacement amplitude of the mass can be derived by (8). Thus, the transmissibility  $T$  can be calculated by the ratio of the displacement amplitude of the mass to that of the base, which can be expressed as

$$T = \sqrt{\left(1 + \hat{X} \cos \theta\right)^2 + \left(\hat{X} \sin \theta\right)^2} / 1 \quad (9)$$

Substituting (6) into (9), the transmissibility  $T$  can be derived as

$$T = \sqrt{1 + \hat{X}^2 + \frac{2\hat{X}}{\beta^2} \left[ (\alpha - \beta^2) \hat{X} + \frac{3}{4} \gamma \hat{X}^3 \right]} \quad (10)$$

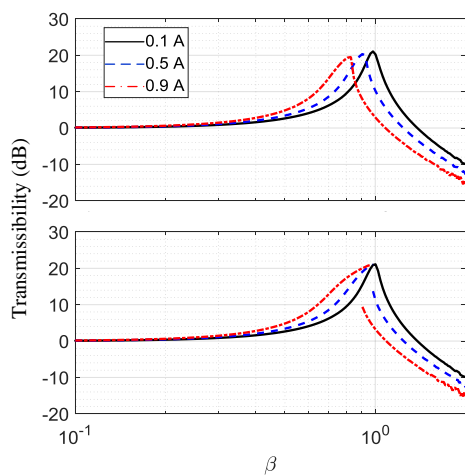


Fig. 5. Simulated transmissibility curves with various currents: (a)  $X_b = 0.5 \text{ mm}$ ; (b)  $X_b = 1.0 \text{ mm}$ .

### C. Nonlinear characteristics

The HSLDS system behaves as a nonlinear system owing to the existence of cubic nonlinearity  $p_3$  [9, 11, 12]. Two sets of numerical simulations with different excitation amplitudes  $X_b$ , namely  $0.5 \text{ mm}$  and  $1.0 \text{ mm}$ , are conducted to illustrate the nonlinearity of the proposed system. All the initial parameters for simulations are listed in Table I. Fig. 5a shows that both the resonance frequency  $\omega_h$  and the peak of transmissibility  $T_h$  decrease with the increase in current when  $X_b = 0.5 \text{ mm}$ . This is explained by the fact that an increase in the current can improve the NS effect, which will be proven experimentally in Section VI-A. However, for the case of  $X_b = 1.0 \text{ mm}$ , the curve-bending and the jumping-down phenomena are observed (see Fig. 5b). This is because a high excitation amplitude may lead to a greater nonlinearity term  $\gamma$  (see (5)). The curve bends toward the right side such that the resonance frequency  $\omega_h$  moves to the high-frequency zone, and the isolation effect diminishes. Notably, it is a hardening system because the curve bends to the right side.

## V. SELECTION OF STRUCTURAL PARAMETERS

The fundamental principal for structural design is to find the optimal structure dimensions that can generate the greatest electromagnetic NS under given conditions. Usually, for HSLDS systems, the greater the generated NS, the lower the equivalent stiffness of the isolator, and hence the lower the natural frequency. In the meanwhile, the peak transmissibility would be lowered because the damping ratio  $\xi$  increases with the decrease in the equivalent stiffness of the isolator. Thus, generating the greatest NS can be achieved by attaining the lowest natural frequency ( $\omega_h$ ) or peak transmissibility ( $T_h$ ). Based on these considerations, in this section,  $\omega_h$  and  $T_h$  are selected as indices to illustrate the influence of the geometric parameters on the vibration isolation performance. To examine the effects more clearly, they are normalized as  $\omega_h/\omega_n$  and  $T_h/T_n$ , respectively. Once the stiffness of the mechanical spring is fixed, the equivalent stiffness of the system is only determined by the electromagnetic stiffness. For

a given layout, the electromagnetic stiffness is entirely affected by the current, geometric parameters, and residual flux density. Appropriate geometric parameters could improve the vibration attenuation performance. Thus, three normalized variables are used to analyze the influences of geometric parameters on  $\omega_h/\omega_n$  and  $T_h/T_n$ : (1) the axial thickness ratio  $R_a = b_w/b_m$ , as shown in Fig. 1c; (2) the radial thickness ratio  $R_r = a_w/a_m$ ; (3) the clearance ratio  $R_g = a_g/a_m$ .

Notably, changing the physical dimensions of the PM would be highly impractical, whereas the geometric dimensions of the CW can be relatively easily altered. Hence, in the following analysis, the dimensions and characteristics of the PMs are fixed, namely,  $r_m = 5 \text{ mm}$ ,  $R_m = 15 \text{ mm}$ ,  $a_m = 10 \text{ mm}$ ,  $b_m = 10 \text{ mm}$ , and  $B_r = 1.35 \text{ T}$ . Other constants for the simulation are  $X_b = 0.5 \text{ mm}$  and  $I_1 = 0.6 \text{ A}$ .

### A. Effect of geometric parameters

*Radial thickness ratio  $R_r$ .* The effect of  $R_r$  is shown in Fig. 6a. With an increase in  $R_r$ , both the normalized peak transmissibility  $T_h/T_n$  and the resonance frequency  $\omega_h/\omega_n$  decrease to some extent. However, when  $R_r > 0.7$ , this trend becomes inconspicuous, which indicates that the increase in  $R_r$  has a slight effect on the peak transmissibility and the resonance frequency. This is because, if  $R_r$  is relatively small, when the PM and current are given, a CW with a larger radial thickness can produce a larger NS. However, once the thickness exceeds a certain limit, it no longer has a significant effect on the NS. With an increase in  $R_r$ , the nonlinearity becomes much stronger and has sufficient strength to distort the curve to the high-frequency band, which may weaken the vibration isolation performance of the system.

*Axial thickness ratio  $R_a$ .* The transmissibility characteristics of the proposed HSLDS isolator with various  $R_a$  values are presented in Fig. 6b. It can be observed that different values of  $R_a$  result in different values of  $\omega_h/\omega_n$  and  $T_h/T_n$ , namely different vibration isolation performances. The shapes of both curves are concave, which signifies that both the peak transmissibility and the resonance frequency become relatively large when the value of  $R_a$  is either too large or too small. Especially, the resonance frequency becomes close to 1, which indicates that the electromagnetic mechanism has almost no effect on the stiffness of the system. This is because there is virtually no NS produced within this size of CWs. Hence,  $R_a$  is a key parameter for designing the system.

*Clearance ratio  $R_g$ .* Fig. 6c shows that a decrease in the clearance results in a decrease in the peak transmissibility and resonance frequency. The reason for this is that a decrease in the clearance between CWs and PMs can make the magnetic induction lines passing through the clearance become much denser, consequently, greater electromagnetic NS will be generated. This is beneficial as greater NS will counteract more stiffness of springs, such that the equivalent stiffness of the system becomes smaller and thus, the resonance frequency decreases. On the contrary, when the ratio increases to a certain extent, the generated NS will be too weak and its effect on the stiffness of system will be neglected and hence, the resonance frequency will be 1, namely, the same as that of the passive

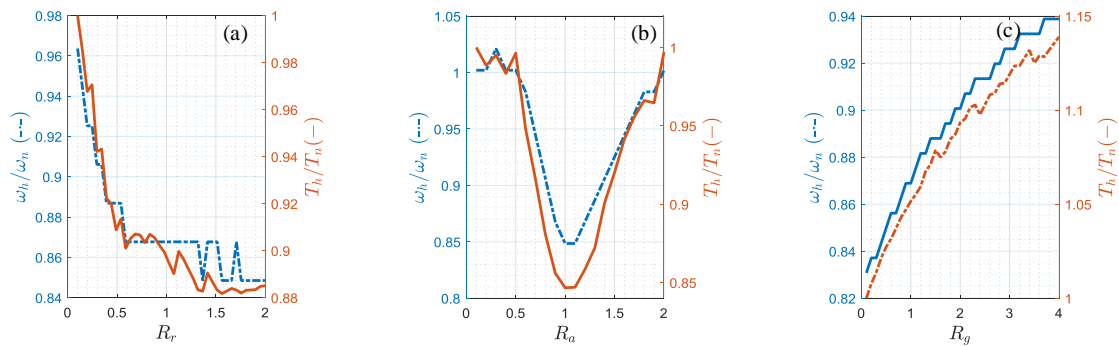


Fig. 6. Simulated resonance frequency and peak transmissibility with various: (a) radial thickness ratios  $R_r$  ( $b_w = 10 \text{ mm}$ ,  $a_g = 0.5 \text{ mm}$ ); (b) axial thickness ratios  $R_a$  ( $a_w = 10 \text{ mm}$ ,  $a_g = 0.5 \text{ mm}$ ); (c) clearance ratios  $R_g$  ( $a_w = 10 \text{ mm}$ ,  $b_w = 10 \text{ mm}$ ).

system (no current in CWs). Hence, it is better to choose a slight clearance for the design. However, the trade-off is that slight clearance requires extreme accuracy of assembling and manufacturing.

### B. Selecting procedure

Judicious selection of the geometric parameters should be exploited in order to realize the design objectives mentioned in Section II, namely, decreasing the natural frequency and lowering the peak transmissibility. Hence, in this section, we will explain how the geometric parameters listed in Table I are obtained.

Based on the analysis in Section V-A, it appears reasonable to decrease the value of  $R_g$ . However, the clearance cannot be always reduced because of the fabricating accuracy and assembling accuracy of CWs and PMs. Therefore, a value of  $R_g = 0.8$  (namely  $a_g = R_g a_m = 0.8 \text{ mm}$ ) is adopted, which is almost the ultimate precision that can be achieved in lab tests. Second, because an increase in the radial thickness ratio  $R_r$  has a slight effect on the transmissibility characteristics if  $R_r > 0.7$ , considering saving copper wires in the CWs and reducing the overall size of the prototype, an  $R_r$  close to  $0.7 \sim 0.8$  is economical. Here,  $R_r = 0.77$  is selected, namely,  $a_w = 0.77 a_m = 7.7 \text{ mm}$ . Thus, we can obtain  $r_c = a_g + R_m = 15.8 \text{ mm}$  and  $R_c = r_c + a_w = 23.5 \text{ mm}$ . Finally, for the axial thickness  $R_a$ , the minimum resonance frequency and peak transmissibility exist when  $R_a$  is  $0.9 \sim 1.1$ , and hence,  $R_a = 1$  (namely  $b_w = R_a b_m = 10 \text{ mm}$ ) is selected as the design parameter for the proposed prototype.

## VI. EXPERIMENTAL RESULTS

### A. Transmissibility results

To compute the transmissibility of the HSLDS system, experiments for different currents were conducted. The white noise was chosen as the excitation signal. The attenuation performance was examined for a payload of  $3.519 \text{ kg}$ . The amplitude of the displacement of the base is  $0.5 \text{ mm}$ . Notably, the relative movement between the CWs and PMs will produce an eddy current damping force. Technically, the damping factors obtained under different relative movements and different current magnitudes are not the same, but the difference can be ignored. Furthermore, in this study, the primary target of the

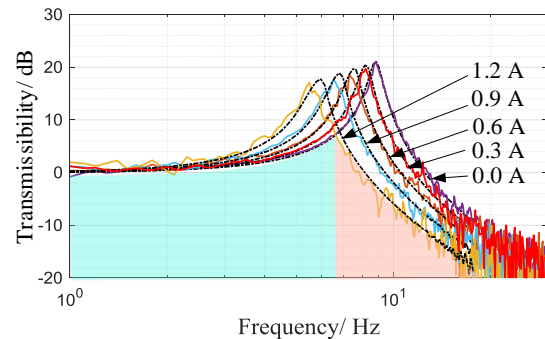


Fig. 7. Experimental results (colored solid) and analytical predictions (black dash-dotted) of transmissibility curves for different current values.

analytical model was to predict whether the NS characteristics would influence the isolation performance, rather than specific damping factors of the system. Thus, the damping coefficient of the system is treated as a constant.

Transmissibility curves measured experimentally (colored solid curves) are illustrated in Fig. 7 alongside the theoretical ones (black dash-dotted curves) computed using (9). When the current increases, the proposed system exhibits considerably improved vibration isolation performance because the resonance frequency is reduced from  $8.80 \text{ Hz}$  to  $5.66 \text{ Hz}$ , and the corresponding zero-crossing point (the starting frequency of the isolation bandwidth) shifts from  $13.0 \text{ Hz}$  to  $7.8 \text{ Hz}$ . Notably,  $1.2 \text{ A}$  is adopted as the upper limit to prevent overheating of the CWs. The experimental results are consistent with the analytical ones in both the low- and high-frequency bands. The results also show that the HSLDS system outperforms the passive system in terms of the vibration attenuation, e.g., the obtained transmissibilities are  $-7.3 \text{ dB}@10 \text{ Hz}$  and  $-15.4 \text{ dB}@15 \text{ Hz}$  for the HSLDS system, whereas they are  $11.3 \text{ dB}@10 \text{ Hz}$  and  $-7.1 \text{ dB}@15 \text{ Hz}$  for the passive system. However, the analytical model overpredicts the resonance frequency and the peak transmissibility because there is an evident discrepancy between the tested result and the theoretical one when the current equals  $1.2 \text{ A}$ . This discrepancy exists probably owing to the slight variation of the damping coefficient and the accuracy of the HB method. Therefore, the divergence between the theoretical prediction and experimental verification is deemed to be acceptable.

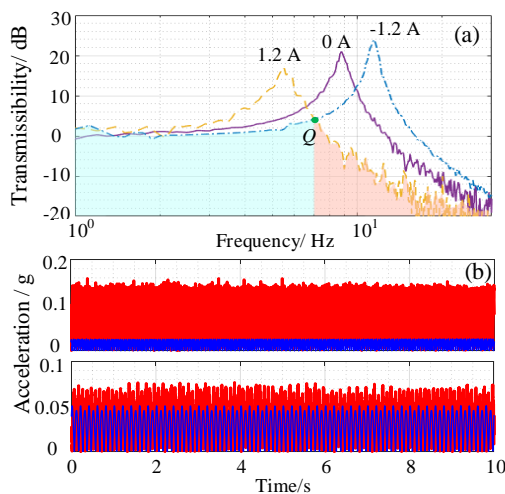


Fig. 8. Experimental results: (a) transmissibility curves; (b) amplitude of acceleration of mass with (blue)/without (red) tuning strategy when the base is subjected to an external excitation with the frequency of  $10\text{ Hz}$  (upper)/ $5\text{ Hz}$  (bottom).

### B. Tuning capability

The experimental results indicate that the transmissibility can be tuned by regulating the current. Fig. 7 also illustrates that, in the low-frequency band (cyan), a high-stiffness system ( $I_1 = 0\text{ A}$ ) has a better vibration attenuation performance than a low-stiffness system ( $I_1 = 1.2\text{ A}$ ). However, the results are opposite in the high-frequency band (orange). This also indicates that: (1) it is preferable to increase the stiffness of the system in the low-frequency band. By modifying the polarity of the current, one can reverse the direction of the electromagnetic force, and subsequently, NS turns into PS. Consequently, the equivalent stiffness increases because it equals the superposition of this PS and the stiffness of springs; (2) a tuning strategy to obtain the best attenuation effect at full frequency band is obtained. To be specific, NS is off in the low-frequency band; instead, an electromagnetic PS is generated by reversing the polarity of the current, and hence the system exhibits a high stiffness behavior. In contrast, in the high-frequency band, NS is on, such that the system exhibits a low stiffness behavior. Please note that we only focus on harmonic base excitations because our main purpose is to obtain the optimal isolation effect for a wide range of excitation frequency through tuning the current, rather than to realize vibration isolation for any types of excitation, such as multi-frequency excitation signals.

Based on these considerations, an ON - OFF tuning strategy is explored to verify the online tuning capability of the proposed HSLDS system. As shown in Fig. 8a, point  $Q$  is the point of intersection of two transmissibility curves when the currents equal  $1.2\text{ A}$  and  $-1.2\text{ A}$  (the minus sign refers to a reversed current), and the corresponding frequency of  $Q$  is  $f_Q = 6.8\text{ Hz}$ . Because payload affects the natural frequency of the isolator, frequency  $f_Q$  should be recalculated for different payloads. When the isolation system is subjected to a sinusoidal base excitation, it will gather the excitation signal and compute the main frequency. If the main frequency is lower

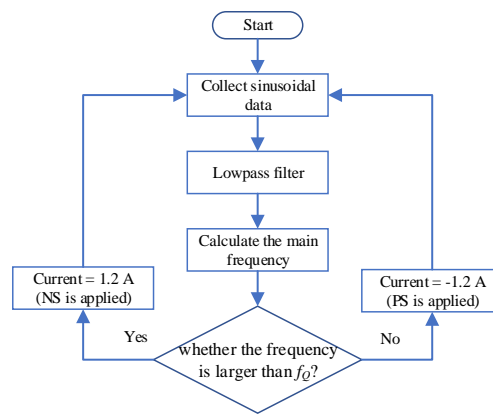


Fig. 9. Flow chart of the proposed stiffness regulation strategy.

than  $f_Q$  (cyan), the current will be set to  $-1.2\text{ A}$ ; otherwise, it will be set to  $1.2\text{ A}$  when the excitation frequency is greater than  $f_Q$  (orange). The detailed procedure of this strategy is illustrated in Fig. 9. Specifically, collecting the sinusoidal data is completed by NI DAQ card PXIe 4497; a lowpass filter with a cut-off frequency  $100\text{ Hz}$  is adopted to recreate the collected data; then, the main frequency component of the collected data is computed through the ‘Power Spectrum’ function and the ‘Peak Search’ function provided by the Sound & Vibration Toolkit of LabVIEW. Finally, the corresponding current is fed into the CWs according to the calculated main frequency.

To verify the proposed tuning strategy, two sets of experiments were carried out. Specifically,  $5\text{ Hz}$  ( $< f_Q$ ) and  $10\text{ Hz}$  ( $> f_Q$ ) were adopted as the excitation frequencies. The results are illustrated in Fig. 8b, where the acceleration responses of the isolated payload of the passive system ( $I_1 = 0\text{ A}$ ) and the system with tuning strategy are illustrated in red and blue, respectively. Fig. 8b shows that the response of the system with tuning (blue) is smaller than the response of the passive system (red). Specifically, the root mean square (RMS) of the acceleration amplitude is reduced by 16.3% (for  $5\text{ Hz}$ ) and 79.8% (for  $10\text{ Hz}$ ). Thus, with the ON - OFF strategy, the system outperforms both the HSLDS system in the low-frequency band and the passive system in the high-frequency band. In other words, this strategy is effective for a wide range of external excitation frequencies.

Transient effect is inevitable during current switching, which can result in displacement overshoot or sudden change in the static position of the payload. For the proposed isolator, electromagnetic stiffness becomes positive when the overshoot exceeds a certain point (details in Section VII), which can help limit the overshoot and prevent instability. Furthermore, Since sudden change in the static position are highly dependent upon the equivalent stiffness, and the lowest equivalent stiffness (at current  $I = 1.2\text{ A}$ ) is still higher than quasi-zero, sudden changes in the static position are within a tolerable range.

Table II presents comparisons between the results obtained from the proposed design and the previous studies, which also focused on the vibration/shock isolation with electromagnetic devices. Even though the proposed isolator has a more compact size, such as a smaller volume (the radial thickness and

TABLE II  
COMPARISON WITH RESULTS OF PREVIOUS STUDIES

Type	Proposed system	Zhou [24]	Ledezma [8, 10]
Layout	Horizontal/Vertical	Horizontal	Horizontal
Range of current	0 ~ 1.2 A	0 ~ 1.2 A	0 A, 2 A
Radial thickness	7.7 mm	10.3 mm	*
Axial thickness	40 mm	88 mm	*
Turns of coil	1152	7130	*
Payload	3.519 kg	0.170 kg	0.075 kg
$\rho$	9254 kg/m <sup>3</sup>	614 kg/m <sup>3</sup>	-
Performance	-7.3 dB@10 Hz -15.4 dB@15 Hz	-6.0 dB@10 Hz	15 dB@10 Hz

\* These values were not provided in Ref. [8, 10].

axial thickness are 7.7 mm and 10×4 mm, respectively) and fewer turns of coils (1152 < 7130), it can bear a heavier load (3.519 > 0.170 > 0.075 kg), which makes it much easier to satisfy engineering requirements. For a more straightforward demonstration of the degree of compactness and load capacity, a so-called *volume loading rate*  $\rho$  is defined.  $\rho$  has the same dimension as density, and it is defined as load carried per unit effective volume (in this case, the effective volume refers to the volume of the part that generates the tunable NS, e.g., volume of CWs). As shown in Table II, the proposed prototype has a considerably large  $\rho$ , which indicates that the vibration isolation for a heavy load can be realized by a small structure. The reason is that, on the surface, the load capacity depends only upon the mechanical springs. Springs with large stiffness (positive) can carry a heavier load. However, in order to achieve the same isolation effect, the system with greater PS should introduce greater NS to neutralize its PS accordingly. This indicates that the proposed system is capable of generating a larger NS with such a compact structure. Thus,  $\rho$  of the proposed design is greater.

In addition, as a power supply is required to energize the CWs, the power consumption is another key criterion that should be considered when evaluating the system. Fig. 10 shows the power consumption at each normalized resonance frequency  $\omega_h/\omega_n$  (See V-A). As  $\omega_h/\omega_n$  shifts to the lower-frequency zone, the consumed power increases. It is no longer a linear relationship because an increase in the power has a much smaller effect upon the reduction of  $\omega_h/\omega_n$ . However, the proposed system consumes the least power for the same  $\omega_h/\omega_n$ , even though its load is the heaviest. The reason is that the resistance of the proposed isolator is lower than that of the other systems. Moreover, the proposed system can generate greater NS with a small current. Thus, the proposed system shows a relatively high efficiency in realizing a similarly scaled vibration attenuation because it requires less power, especially at  $\omega_h/\omega_n < 0.75$ .

## VII. DISCUSSION

The above sections focused on realizing vibration attenuation from the perspective of tuning the magnitude of the stiffness. However, as the HSLDS system behaves as a nonlinear system, we can also realize vibration attenuation from the standpoint of tuning the nonlinearity. In Section IV-C, weak nonlinearity is favorable for the hardening system because of

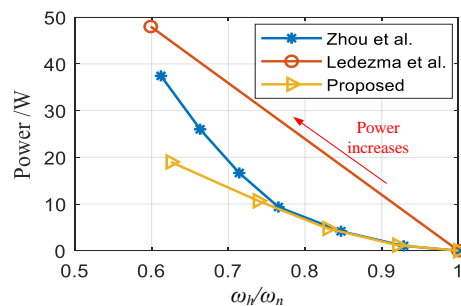


Fig. 10. Consumed power of electromagnetic mechanisms measured using experiments.

the curve-bending phenomenon induced by the strong nonlinearity of NS. The more the system approximates to a linear system, the smaller the  $\gamma$  will be. Thus, from the perspective of the vibration attenuation, a smaller  $\gamma$  is appropriate. Inspired by the Helmholtz coil [31], we can obtain a linear system by producing an approximate uniform magnetic field. For our proposed system, this can be achieved by enlarging the axial clearance (denoted by  $D_a$ ) between adjacent windings. An example is shown in Fig. 11.

We obtain two force–displacement curves (as illustrated in Fig. 11a) with the same  $\alpha$  but different  $\gamma$  by precisely tuning  $I_1$  and  $D_a$ . When  $I_1 = 1.55$  A and  $D_a = 10$  mm (the red curve in Fig. 11a), the force–displacement curve is an approximate straight line, which indicates that the system is close to a linear system. This is because, if the produced magnetic field is uniform, the nonlinearity of NS will be eliminated. Therefore, the effect of the nonlinearity term  $\gamma$  can be neglected as it is too small. When  $I_1 = 1.2$  A and  $D_a = 0$  mm (the blue curve in Fig. 11a),  $\gamma$  cannot be neglected and hence, the force–displacement curve is nonlinear. The simulation results of transmissibilities also reveal the advantage of small  $\gamma$  (the red curve in Fig. 11b) because it shows that the resonance frequency shifts to the left slightly for a smaller  $\gamma$ .

In addition, mechanical stability is also important to HSLDS isolators, especially when deformation is too large. For the proposed system, the electromagnetic stiffness within about  $\pm 5.5$  mm is negative (see Fig. 12b). This range is determined by the dimensions of the electromagnetic mechanism, and optimal isolation performance can be achieved within this range because the equivalent stiffness is reduced. Beyond this range, the electromagnetic stiffness becomes positive. Therefore, even if the deformation is too large, it is not possible for the equivalent stiffness to become negative and the positive electromagnetic stiffness can ensure the mechanical stability of the proposed system.

## VIII. CONCLUSION

This paper proposed an HSLDS isolator with a tunable NS. The NS is provided by a nesting-type electromagnetic mechanism that consists of four coaxial CWs and four ring PMs. The NS is combined in parallel with the PS produced by mechanical springs. The equivalent stiffness of the isolator is expressed as the superposition of the PS and the NS. By tuning the magnitude of the current, the equivalent stiffness

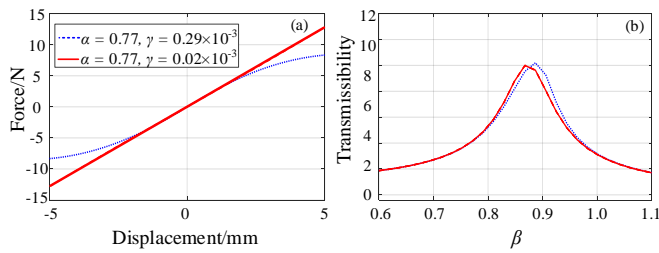


Fig. 11. Simulated results: (a) force–displacement curve; (b) transmissibility under two different conditions. ( $b_m = 10 \text{ mm}$ ,  $b_w = 10 \text{ mm}$ ,  $B_r = 1.35 \text{ T}$ ,  $N_z = 18$ ,  $X_b = 5 \text{ mm}$ ,  $a_g = 0.5 \text{ mm}$ ,  $r_c = 15.8 \text{ mm}$ ,  $R_c = 23.5 \text{ mm}$ ,  $r_m = 5 \text{ mm}$  and  $R_m = 15 \text{ mm}$ ).

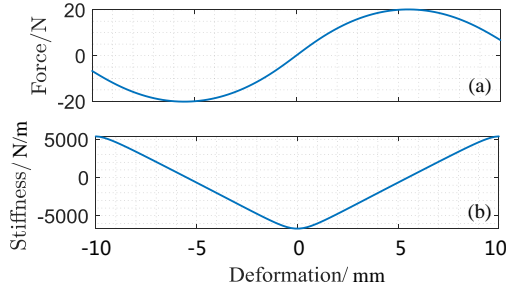


Fig. 12. Simulated (a) electromagnetic force and (b) stiffness when  $I = 1.2 \text{ A}$ .

can be adjusted dynamically. The calculation of the interaction force/stiffness is achievable using the Amperian current model. The motion equation and transmissibility characteristics of the isolator were set up and analyzed in detail. Both the numerical simulation analysis and experimental results show that the isolator can realize better performance than passive system. Compared with previous studies, the proposed isolator has three outstanding advantages, i.e., a more compact structure, heavier load capacity, and higher efficiency.

#### APPENDIX

The axial force between two coaxial filaments is given by

$$F_a(r_1, r_2, L) = \mu_0 I_1 I_2 L \sqrt{\frac{k^2}{4r_1 r_2}} \left[ K - \frac{1}{2} \frac{k^2 - 1}{k^2 - 1} E \right] \quad (\text{A.1})$$

where  $K$  and  $E$  are the complete first and second elliptic integrals with modulus  $k^2$ , respectively, and

$$k^2 = \frac{4r_1 r_2}{(r_1 + r_2)^2 + L^2} \quad (\text{A.2})$$

Four steps are used to calculate the interaction force exerted between CWs and ring PMs. First, each turn of the CW is considered as a separate coil (the filament) with current  $I_1$ . Second, the ring PM is considered as two cylindrical magnets whose radii equal  $R_m$  and  $r_m$ . Third, the arrangement of “turns” used to model the cylindrical PM is related to an equivalent surface current density; specifically, the equivalent current in each filament is  $I_2 = B_r b_m / (N_m \mu_0)$ , and the number of “turns”  $N_m$  should be sufficiently large to ensure that the calculation result converges to a stable value. Finally, the total force between a CW and a ring PM can be expressed as a superposition of every pair of filaments

$$F_{CM} = F_1 + F_2 \quad (\text{A.3})$$

where

$$F_1 = - \sum_{n_m=1}^{N_m} \sum_{n_r=1}^{N_r} \sum_{n_z=1}^{N_z} F_a(r(n_r), r_m, L(n_m, n_z)) \quad (\text{A.4})$$

$$F_2 = \sum_{n_m=1}^{N_m} \sum_{n_r=1}^{N_r} \sum_{n_z=1}^{N_z} F_a(r(n_r), R_m, L(n_m, n_z)) \quad (\text{A.5})$$

$$r = r_c + \frac{n_r - 1}{N_r - 1} (R_c - r_c) \quad (\text{A.6})$$

$$L = x - \frac{1}{2} (b_c + b_m) + \frac{n_z - 1}{N_z - 1} b_c + \frac{N_m - n_m}{N_m - 1} b_m \quad (\text{A.7})$$

The sign of the force is determined by the directions of the (equivalent) current. If the direction of the applied force exerted on the PM is identical to the positive direction of the  $x$  axis, the force is positive, and vice versa. NS can be obtained by differentiating  $F_{CM}$  with respect to the relative displacement  $x$ , namely,  $-\partial F / \partial x$ . The minus sign is introduced in the expression because the restoring force produced by the NS system is opposite to the electromagnetic force.

#### REFERENCES

- [1] M. H. Kim, H. Y. Kim, H. C. Kim, and D. Ahn, “Design and control of a 6-dof active vibration isolation system using a halbach magnet array,” *IEEE/ASME Trans. Mechatron.*, vol. 21, no. 4, pp. 2185–2196, 2016.
- [2] G. Smutzer, H. Desai, S. E. Coldwell, and J. W. Griffith, “Comparison and classification of high-precision actuators based on stiffness influencing vibration isolation,” *IEEE/ASME Trans. Mechatron.*, vol. 21, no. 2, pp. 1169–1178, 2016.
- [3] E. Csencsics, M. Thier, R. Hainisch, and G. Schitter, “System and control design of a voice coil actuated mechanically decoupling two-body vibration isolation system,” *IEEE/ASME Trans. Mechatron.*, vol. 23, no. 1, pp. 321–330, 2017.
- [4] B. Yan, K. Wang, C. Kang, X. Zhang, and C. Wu, “Self-sensing electromagnetic transducer for vibration control of space antenna reflector,” *IEEE/ASME Trans. Mechatron.*, vol. 22, no. 5, pp. 1944–1951, 2017.
- [5] S. Guo, L. Xu, Y. Liu, X. Guo, and L. Zuo, “Modeling and experiments of a hydraulic electromagnetic energy harvesting shock absorber,” *IEEE/ASME Trans. Mechatron.*, vol. 22, no. 6, pp. 2684–2694, 2017.
- [6] A. J. Mcdaid and B. R. Mace, “A robust adaptive tuned vibration absorber using semi-passive shunt electronics,” *IEEE Trans. Ind. Electron.*, vol. 63, no. 8, pp. 5069–5077, 2016.
- [7] J. Ding, X. Luo, X. Chen, O. Bai, and B. Han, “Design of active controller for low-frequency vibration isolation considering noise levels of bandwidth-extended absolute velocity sensors,” *IEEE/ASME Trans. Mechatron.*, vol. 22, no. 4, pp. 1832–1842, 2018.
- [8] D. F. Ledezma, N. S. Ferguson, and M. J. Brennan, “An experimental switchable stiffness device for shock

- isolation,” *J. Sound Vib.*, vol. 331, no. 23, pp. 4987–5001, 2012.
- [9] Y. Zheng, X. Zhang, Y. Luo, B. Yan, and C. Ma, “Design and experiment of a high-static-low-dynamic stiffness isolator using a negative stiffness magnetic spring,” *J. Sound Vib.*, vol. 360, pp. 31–52, 2016.
- [10] D. F. Ledezma, N. S. Ferguson, and M. J. Brennan, “Shock isolation using an isolator with switchable stiffness,” *J. Sound Vib.*, vol. 330, no. 5, pp. 868–882, 2011.
- [11] A. Carrella, M. J. Brennan, T. P. Waters, and V. L. Jr, “Force and displacement transmissibility of a nonlinear isolator with high-static-low-dynamic-stiffness,” *Int. J. Mech. Sci.*, vol. 55, no. 1, pp. 22–29, 2012.
- [12] Z. Lu, M. J. Brennan, and L. Q. Chen, “On the transmissibilities of nonlinear vibration isolation system,” *J. Sound Vib.*, vol. 375, pp. 28–37, 2016.
- [13] X. Sun, X. Jing, J. Xu, and L. Cheng, “A quasi-zero-stiffness-based sensor system in vibration measurement,” *IEEE Trans. Ind. Electron.*, vol. 61, no. 10, pp. 5606–5614, 2014.
- [14] T. D. Le, M. T. N. Bui, and K. K. Ahn, “Improvement of vibration isolation performance of isolation system using negative stiffness structure,” *IEEE/ASME Trans. Mechatron.*, vol. 21, no. 3, pp. 1561–1571, 2016.
- [15] X. Jing, Y. Wang, Q. Li, and X. Sun, “Design of a quasi-zero-stiffness based sensor system for the measurement of absolute vibration displacement of moving platforms,” *Smart Mater. Struct.*, vol. 25, no. 9, pp. 097 002–097 014, 2016.
- [16] Y. Zheng, X. Zhang, Y. Luo, Y. Zhang, and S. Xie, “Analytical study of a quasi-zero stiffness coupling using a torsion magnetic spring with negative stiffness,” *Mech. Syst. Sig. Process.*, vol. 100, pp. 135–151, 2018.
- [17] A. Carrella, M. J. Brennan, I. Kovacic, and T. P. Waters, “On the force transmissibility of a vibration isolator with quasi-zero-stiffness,” *J. Sound Vib.*, vol. 322, no. 4, pp. 707–717, 2009.
- [18] B. Yan, H. Ma, C. Zhao, C. Wu, K. Wang, and P. Wang, “A vari-stiffness nonlinear isolator with magnetic effects: Theoretical modeling and experimental verification,” *Int. J. Mech. Sci.*, vol. 148, pp. 745–755, 2018.
- [19] G. Dong, X. Zhang, S. Xie, B. Yan, and Y. Luo, “Simulated and experimental studies on a high-static-low-dynamic stiffness isolator using magnetic negative stiffness spring,” *Mech. Syst. Signal Pr.*, vol. 86, pp. 188–203, 2017.
- [20] D. Xu, Q. Yu, J. Zhou, and S. R. Bishop, “Theoretical and experimental analyses of a nonlinear magnetic vibration isolator with quasi-zero-stiffness characteristic,” *J. Sound Vib.*, vol. 332, no. 14, pp. 3377–3389, 2013.
- [21] C. Cheng, S. Li, Y. Wang, and X. Jiang, “Force and displacement transmissibility of a quasi-zero stiffness vibration isolator with geometric nonlinear damping,” *Nonlinear Dyn.*, vol. 87, no. 4, pp. 1–13, 2016.
- [22] C. B. Churchill, D. W. Shahan, S. P. Smith, A. C. Keefe, and G. P. Mcknight, “Dynamically variable negative stiffness structures,” *Sci. Adv.*, vol. 2, no. 2, p. e1500778, 2016.
- [23] D. Ledezma, J. J. Villalobos-Luna, N. Ferguson, and M. Brennan, “Theoretical and experimental analysis of shock isolation using non linear stiffness,” *J. Acoust. Soc. Am.*, vol. 134, no. 5, pp. 4197–4197, 2013.
- [24] N. Zhou and K. Liu, “A tunable high-static-low-dynamic stiffness vibration isolator,” *J. Sound Vib.*, vol. 329, no. 9, pp. 1254–1273, 2010.
- [25] —, “Characterization of an electromagnetic vibration isolator,” *J. Electromagn. Anal. Appl.*, vol. 3, no. 12, pp. 519–528, 2011.
- [26] H. Pu, S. Yuan, Y. Peng, K. Meng, J. Zhao, R. Xie, Y. Huang, Y. Sun, Y. Yang, S. Xie, J. Luo, and X. Chen, “Multi-layer electromagnetic spring with tunable negative stiffness for semi-active vibration isolation,” *Mech. Syst. Sig. Process.*, vol. 121, pp. 942–960, 2019.
- [27] B. W. Robertson and A. Zander, “Axial force between a thick coil and a cylindrical permanent magnet: Optimizing the geometry of an electromagnetic actuator,” *IEEE Trans. Magn.*, vol. 48, no. 9, pp. 2479–2487, 2012.
- [28] R. Ravaut, G. Lemarquand, S. Babic, V. Lemarquand, and C. Akyel, “Cylindrical magnets and coils: Fields, forces, and inductances,” *IEEE Trans Magn*, vol. 46, no. 9, pp. 3585–3590, 2010.
- [29] A. Shiri and A. Shoulaie, “A new methodology for magnetic force calculations between planar spiral coils,” *Prog. Electromagn. Res.*, vol. 95, no. 4, pp. 39–57, 2009.
- [30] J. T. Conway, “Inductance calculations for noncoaxial coils using bessel functions,” *IEEE Trans. Magn.*, vol. 43, no. 3, pp. 1023–1034, 2007.
- [31] R. Beiranvand, “Effects of the winding cross section shape on the magnetic field uniformity of the high field circular helmholtz coil systems,” *IEEE Trans. Ind. Electron*, vol. 64, no. 9, pp. 7120–7131, 2017.



His research interests include robotics and vibration controlling.

**Yi Sun** received his B.Eng degrees in Mechanical Engineering in 2003, and M.Eng degree in Mechatronic Engineering in 2006, all from Huazhong University of Science and Technology (Wuhan, China). In 2013, he received his Dr.Eng degree in Robotics from Ritsumeikan University (Kyoto, Japan). From 2013 to 2016 he worked as a senior researcher at Ritsumeikan University. In July 2016, granted by the Program of Young Eastern Scholar of Shanghai, he joined Shanghai University as an Assistant Professor.



**Jinglei Zhao** received both B.Eng. degree and M.Eng degree in Mechanical Engineering from Shanghai University (Shanghai, China) in 2012 and 2015. He has been a doctoral candidate at Shanghai University (Shanghai, China) since 2017. His research interests include modeling of nonlinear vibration isolation systems.



**Min Wang** received his B.Eng and M.Eng degree in Mechatronic Engineering in 2012, all from Wuhan University of Technology (Wuhan, China) in School of Mechanical and Electronic Engineering. In 2018, he received his Dr.Eng degree in Vibration Isolation and Active Control from Huazhong University of Science and Technology (Wuhan, China). He is now working as a lecturer in Shanghai University, and his research interests include vibration isolation and vibration controlling.



**Yan Peng** received the Ph.D. degree in pattern recognition and intelligent systems from Shenyang Institute of Automation, Chinese Academy of Sciences (Shenyang, China) in 2009. She is currently a Professor with Shanghai University (Shanghai, China) where she is the Executive Dean of the Research Institute of USV Engineering. Her current research interests include modeling and control of unmanned surface vehicles, field robotics, and locomotion systems.



**Yu Sun** received the B.S. degree in electrical engineering from Dalian University of Technology, Dalian, China, in 1996, the M.S. degree from the Institute of Automation, Chinese Academy of Sciences, Beijing, China, in 1999, and the M.S. degree in electrical engineering and the Ph.D. degree in mechanical engineering from the University of Minnesota, Minneapolis, MN, USA, in 2001 and 2003, respectively. He is a Professor with the Department of Mechanical and Industrial Engineering and is jointly appointed

with the Institute of Biomaterials and Biomedical Engineering and the Department of Electrical and Computer Engineering, University of Toronto, Toronto, ON, Canada. He is the Canada Research Chair in Micro and Nano Engineering Systems. His research areas include the design and fabrication of M/NEMS devices, micronanorobotic manipulation, and the manipulation and characterization of cells, biomolecules, and nanomaterials.



**Shaorong Xie** received the B. Eng. and M. Eng. degrees in mechanical engineering from Tianjin Polytechnic University (Tianjin, China) in 1995 and 1998, respectively, and the Dr. Eng. degree in mechanical engineering from the Institute of Intelligent Machines at Tianjin University and the Institute of Robotics and Automatic Information System, Nankai University (Tianjin, China) in 2001. She is a Professor with the School of Mechatronic Engineering and Automation, Shanghai University (Shanghai, China). Her research areas include

advanced robotics technologies, bionic control mechanisms of eye movements, and image monitoring systems.



**Huayan Pu** received the M.Sc. and Ph.D. degrees in mechatronics engineering from Huazhong University of Science and Technology (Wuhan, China) in 2007 and 2011, respectively. Currently, she is a Professor at Shanghai University (Shanghai, China). Her current research interests include vibration controlling and robotics. Dr. Pu was awarded the best paper in biomimetics at the 2013 IEEE International Conference on Robotics and Biomimetics. She was also nominated as the best conference paper

finalist at the 2012 IEEE International Conference on Robotics and Biomimetics.



**Jun Luo** received the B.S. and M.S. degrees in mechanical engineering from Henan Polytechnic University (Jiaozuo, China) in 1994 and 1997, respectively, and the Ph.D. degree from the Research Institute of Robotics, Shanghai Jiao Tong University (Shanghai, China) in 2000. He is a Professor in the School of Mechatronics Engineering and Automation, Shanghai University (Shanghai, China). He is the Head of the Precision Mechanical Engineering Department at Shanghai University and Vice Director of the

Shanghai Municipal Key Laboratory of Robotics. His research areas include robot sensing, sensory feedback, mechatronics, man-machine interfaces, and special robotics.



**Yi Yang** received his Doctoral degree in Mechanical Engineering from Beihang University (Beijing, China) in 2012. He has been an associate professor at Shanghai University (Shanghai, China) since 2016. His research interests include designing, modeling and synthesizing of mechanical systems.